

# Design and Performance of the Wide-Field X-Ray Monitor on Board the High-Energy Transient Explorer 2

Yuji SHIRASAKI,<sup>1,2</sup> Nobuyuki KAWAI,<sup>2,3</sup> Atsumasa YOSHIDA,<sup>2,4</sup> Masaru MATSUOKA,<sup>5</sup>  
Toru TAMAGAWA,<sup>2</sup> Ken'ichi TORII,<sup>2</sup> Takanori SAKAMOTO,<sup>2,3</sup> Motoko SUZUKI,<sup>3</sup>  
Yuji URATA,<sup>2,3</sup> Rie SATO,<sup>3</sup> Yujin NAKAGAWA,<sup>4</sup> Daiki TAKAHASHI,<sup>4</sup>  
Edward E. FENIMORE,<sup>6</sup> Mark GALASSI,<sup>6</sup> Donald Q. LAMB,<sup>7</sup> Carlo GRAZIANI,<sup>7</sup>  
Timothy Q. DONAGHY,<sup>7</sup> Roland VANDERSPEK,<sup>8</sup>  
Makoto YAMAUCHI,<sup>9</sup> Kunio TAKAGISHI,<sup>9</sup> and Isamu HATSUKADE<sup>9</sup>

<sup>1</sup>*National Astronomical Observatory of Japan, Osawa, Mitaka, Tokyo 181-8588*  
*yuji.shirasaki@nao.ac.jp*

<sup>2</sup>*RIKEN, Hirosawa, Wako, Saitama 351-0198*

<sup>3</sup>*Department of Physics, Tokyo Institute of Technology, Meguro-ku, Tokyo 152-8551*

<sup>4</sup>*Department of Physics, Aoyama Gakuin University, Sagamihara, Kanagawa 229-8558*

<sup>5</sup>*NASDA, Tsukuba, Ibaraki 304-8505*

<sup>6</sup>*Los Alamos National Laboratory, Los Alamos, NM 87545, USA*

<sup>7</sup>*Department of Astronomy and Astrophysics, University of Chicago, Chicago, IL 60637, USA*

<sup>8</sup>*MIT/CSR 77 Massachusetts Avenue, Cambridge, MA 02139, USA*

<sup>9</sup>*Faculty of Engineering, Miyazaki University, Miyazaki 889-2192*

(Received 2003 May 7; accepted 2003 July 8)

## Abstract

The Wide-field X-ray Monitor (WXM) is one of the scientific instruments carried on the High Energy Transient Explorer 2 (HETE-2) satellite launched on 2000 October 9. HETE-2 is an international mission consisting of a small satellite dedicated to provide broad-band observations and accurate localizations of gamma-ray bursts (GRBs). A unique feature of this mission is its capability to determine and transmit GRB coordinates in almost real-time through the burst alert network. The WXM consists of three elements: four identical Xe-filled one-dimensional position-sensitive proportional counters, two sets of one-dimensional coded apertures, and the main electronics. The WXM counters are sensitive to X-rays between 2 keV and 25 keV within a field-of-view of about 1.5 sr, with a total detector area of about 350 cm<sup>2</sup>. The in-flight triggering and localization capability can produce a real-time GRB location of several to 30 arcmin accuracy, with a limiting sensitivity of 10<sup>-7</sup> erg cm<sup>-2</sup>. In this report, the details of the mechanical structure, electronics, on-board software, ground and in-flight calibration, and in-flight performance of the WXM are discussed.

**Key words:** space vehicles: instruments — instrumentation: detector — instrumentation: proportional counter — gamma rays: bursts — X-rays: bursts

## 1. Introduction

The origin and nature of Gamma-ray bursts (GRBs) has been one of the outstanding mysteries of astrophysics since the phenomenon was discovered in the 1970s. The discovery of GRB afterglows by the BeppoSAX X-ray satellite (Costa et al. 1997) produced a breakthrough in the study of GRB. Since the discovery, follow-up observations of many GRB afterglows have been successfully performed. The observations have furnished strong evidence that at least the long class of GRB originates from explosions of super-massive stars at cosmological distances. The HETE-2 (Ricker et al. 2003) is the first satellite dedicated to GRB observations and is intended to provide the astronomical community with prompt, high-accuracy GRB positions — a few tens of arcminutes to a few tens of arcseconds, with delay times of 10 s to a few hours. This capability not only increases the number of detected GRB counterparts, but also provides an opportunity for multi-wavelength observations of GRBs in their very early phase. Such observations were nearly impossible prior to the HETE-2 era.

The HETE-2 instrument complement consists of three scientific instruments: the French Gamma Telescope (FREGATE), the Wide-field X-ray Monitor (WXM), and the Soft X-ray Camera (SXC). FREGATE (Atteia et al. 2003) consists of four identical scintillation detectors. It is sensitive to photons with energies from 6 to 400 keV. It is responsible for triggering and spectroscopy in the hard X-ray and Gamma-ray energy ranges. Its field of view is  $70^\circ$  (half width at zero maximum) and its total detection area is  $160 \text{ cm}^2$ . The SXC (Villasenor et al. 2003) is a 1-D coded mask system using MIT-LL CCID-20's as the detecting elements, and is sensitive to photons with energies from 500 eV to 14 keV, with 2% resolution at 6 keV and with a position resolution of  $10''$  for bright bursts (1 Crab; 10 s). SXC's total detection area is  $75 \text{ cm}^2$  and its field of view is  $65^\circ$  (full width at zero maximum). The WXM, on the other hand, has a detection area of  $352 \text{ cm}^2$  and a field of view of  $80^\circ$  (FWZM). Thus, the WXM is more sensitive to weak bursts than the SXC, and the two X-ray instruments play a complementary role to each other, balancing detection sensitivity against location resolution.

## 2. The WXM Instrument

### 2.1. General Properties of the WXM

The WXM instrument is located at the center of the spacecraft, as shown in figure 1. The HETE-2 spacecraft is in an equatorial orbit, with an inclination angle of  $2^\circ$  and a 600 km altitude. The instruments usually point toward the anti-sun direction. Consequently, the WXM field of view ( $80^\circ \times 80^\circ$ ) moves along the ecliptic and is obstructed by the earth on the

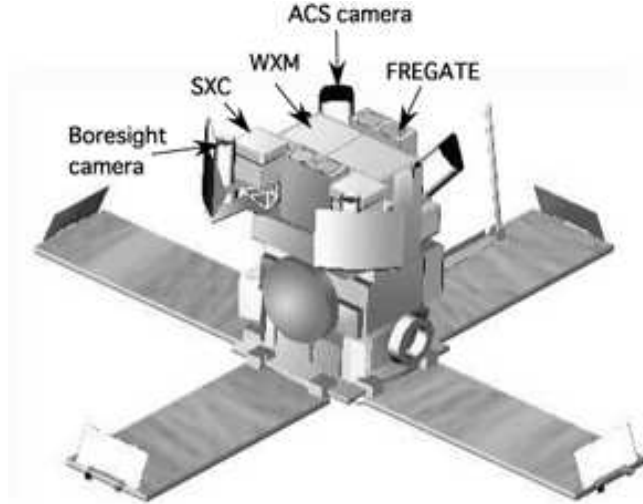


**Fig. 1.** Schematic drawing of the HETE-2 spacecraft.

day side of the orbit.

The WXM consists of two units, the X-camera and the Y-camera. Each camera consists of two identical one-dimensional position-sensitive proportional counters, placed 187 mm beneath a one-dimensional coded-aperture mask. The PSPCs in the X-camera are referred to as XA and XB, while those in the Y-camera are referred to as YA and YB. The orientation of the PSPCs and the mask of the X-camera is perpendicular to the orientation of the PSPCs and the mask of the Y-camera, so that the X Y locations of GRBs are determined separately. Each proportional counter has three anode channels, which are referred to as XA0, XA1, and XA2 for the case of the XA counter, and similarly for the other counters.

One unit consists of a one-dimensional coded mask and two 1-D position-sensitive proportional counters (PSPCs) placed 187 mm below the mask. The area of each coded mask is twice that of the total detector area, to ensure a wide field of view. The masks are supported by an aluminum support structure. Each coded mask consists of a plate of aluminum (0.5 mm thickness) plated with gold (50.8  $\mu\text{m}$ ) with a series of slits whose widths are randomly varying integer multiples of 2 mm. The open fraction of the mask is 0.33. A 7.6  $\mu\text{m}$  thickness aluminum coated kapton foil is placed in front of the mask, as a thermal shield. The WXM instrument schematic drawing is shown in figure 3. The field of view of the X unit is geometrically limited to  $\theta_x = -38^\circ$  to  $+40^\circ$  and  $\theta_y = -44^\circ$  to  $+44^\circ$ , while that of the Y unit is limited to  $\theta_x = -46^\circ$  to  $+43^\circ$  and  $\theta_y = -39^\circ$  to  $+39^\circ$ , where  $\theta_x$  and  $\theta_y$  are the projection angles measured from the vertical direction onto the XZ and YZ plane of the detector coordinate system, respectively. The location of a GRB is determined by independently measuring a set of two shift distances of the mask pattern shadow on the X and Y detectors.

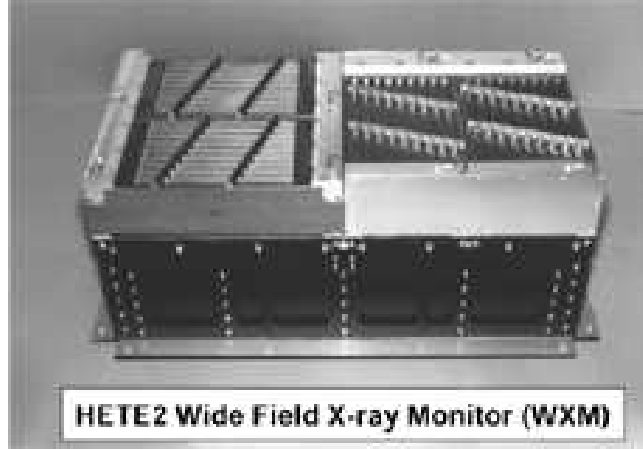


**Fig. 2.** Photograph of the WXM detector. Four proportional counters are attached to the electronics box. The X detector is comprised of the left two counters. It measures the projection angle of the burst direction in the XZ plane. The Y detector is comprised of the right two counters. It measures the projection angle in the YZ plane. The Z axis is along the vertical direction in the picture, while X axis points from right to left. The X detector consists of the XA (far side) and XB detectors (near side), while the Y detector consists of the YA (left) and YB (right) detectors.

## 2.2. Proportional Counter of the WXM

Each PSPC has three anode wires, each composed of a carbon fiber  $10\ \mu\text{m}$  in diameter and 120 mm in length. Each PSPC also has four veto wires of gold-plated tungsten,  $20\ \mu\text{m}$  in diameter. The measured resistance of the carbon fibers ranges from 12.0 to 15.8 k $\Omega$ . The advantage of using carbon fiber is its ability to withstand an electric discharge without damage. We have tested this durability using an X-ray generator, and confirmed that the performance is not changed even after strong X-ray irradiation comparable in strength to an X4-class solar flare.

As shown in figure 4, the inside of the counter is divided into an upper layer consisting of three anode cells and a lower veto layer. Most of the X-rays are absorbed in the upper cells and produce a signal on one of the anodes, while charged particles ionize the Xe gas along their trajectories and produce signals on multiple wires. The three upper cells are partitioned by  $50\ \mu\text{m}$  diameter tungsten cathode wires placed at intervals of 3 mm. The counters are filled with xenon (97%) and carbon dioxide (3%) at 1.4 atm pressure at room temperature. They have beryllium entrance windows of  $100\ \mu\text{m}$  thickness. The detector body is made of grade-2 titanium and supported against an internal pressure by parallel and slant bars. The slant bar is designed to avoid complete obscuration of a detector mask element. The geometrical area of the entrance windows is 88 cm<sup>2</sup>. Its effective area as a function of the energy is shown in figure 5 for vertical X-ray incidence.

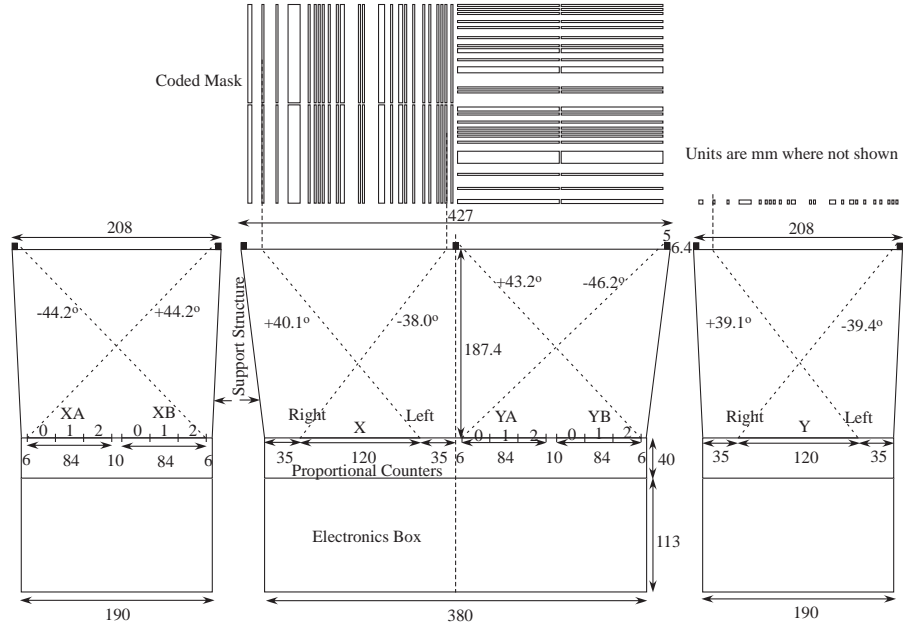


**Fig. 3.** WXM instrument schematic drawing. A coded mask is placed at 187.37 mm above the proportional counters and supported by an aluminum structure. The field of view is restricted by masks and fasteners, which fix the coded mask on the support structure.

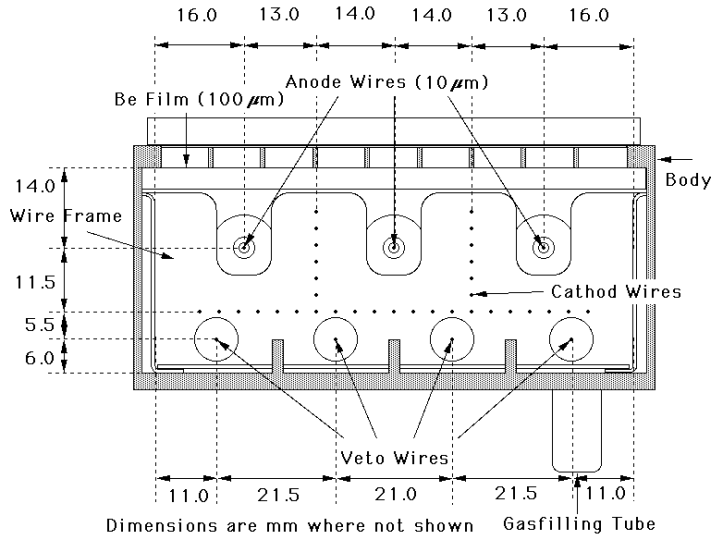


**Fig. 4.** Cross section of a PSPC of WXM. The anode wires in the three upper cells are for X-ray detection and those in the lower cells for rejection of charged particle events by the anti-coincidence method. The 120 mm×83.5 mm entrance window is sealed by a 100 μm Be film.

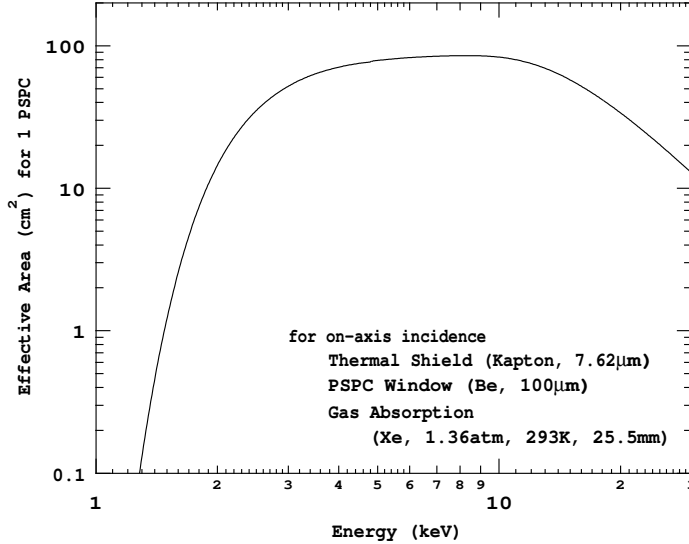


**Fig. 5.** Calculated effective area of one PSPC for on-axis X-ray incidence. Absorption by thermal shield and Be window, and stopping probability in the Xe(97%)+CO<sub>2</sub>(3%) mixture gas are taken into account. The maximum is 85.4 cm<sup>2</sup> at 8.3 keV.

### 2.3. Electronics and Processing

A block diagram of WXM signal processing is shown in figure 6. Analog signals from both ends of the anodes are processed separately by charge-sensitive preamplifiers (Amptek A225), while the signals from the four veto anodes are summed before the processing. Seven A225s are used for each counter. The output of each A225 is connected to peak-hold (P/H) and lower-level discriminator (LD) circuits through a main amplifier. The gain of the main amplifier is adjustable to 32 levels with a dynamic range of 10, except for the veto signal. The LD level is selectable from 4 levels of 100, 140, 200, 500 AD units (which correspond to 0.4, 0.6, 0.9, and 2.5 keV, respectively), for a standard operation mode and for X-ray incidence at the center of the anode.

The logic for the AD conversion starts when any one of the anode signals exceeds the lower discrimination level. AD conversion is performed only for the anode which has generated a LD signal. In the case of an LD hit for multiple anodes, one anode is selected by a pre-determined priority (wire 1 > 0 > 2). In this way, pulse heights induced at both the left and right sides of an anode are digitized to 12-bit precision. Event data is expressed in two 16-bit words, comprising 2×12-bit of ADU, 2-bit of counter ID, 4-bit of hit pattern flag representing the LD hit for the 3 anodes and one veto, and two 1-bit word order flags. Background events caused by charged cosmic rays are identified as multiple anodes/veto hit events, and can be rejected using the hit pattern flag.

The data loaded on the shift register is transmitted to the X-DSP after the previous data transmission is complete. In view of the fact that the data transfer time is 32 μs and

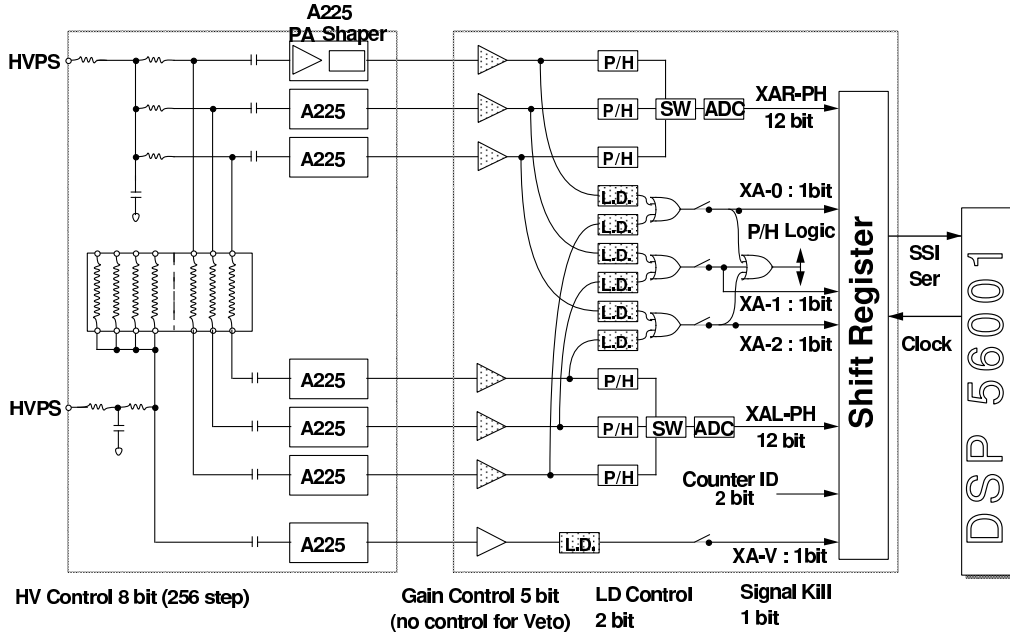


**Fig. 6.** WXM signal processing scheme for one counter. The same scheme applies to all four counters. Details are described in the text.

signal processing time is  $\sim 20 \mu\text{s}$ , we can estimate that even for a count rate of  $12500 \text{ c s}^{-1}$  the dead time fraction is at most 10%. If more than one detector is waiting to transfer data, one of them is selected by a round-robin cyclic priority. This cyclic priority scheme assures that the data can be taken uniformly for all of the detectors, even when one of the detectors has a much higher count rate due to an anomalous condition such as electric discharge.

#### 2.4. CPU Processing

The spacecraft computer system consists of four identical processor boards: each board contains one transputer (INMOS T805), two Digital Signal Processor (Motorola, DSP56001), and 20 Mbytes RAM. The processors are assigned to the spacecraft and science nodes in the following way: node 0: spacecraft processing, node 1: SXC, node 2: optical cameras, node 3: WXM and Fregate. The “links” feature of the transputer allows for quick and efficient communications between processors. The DSP serves as an interface to the instrument.

The WXM and FREGATE share a common processor board (XG node), and each has a dedicated DSP (X-DSP and G-DSP) for handling the event data from the instruments, producing various data products and commanding the instruments. For the safety of the detector, the X-DSP provides a self-safety mechanism to the WXM: an HV shutdown command is executed when the total count rate exceeds 20000 counts per 4 s, or when the count rate in one of the four counters goes down below 5 counts per 0.8 s.

The data products generated on the X-DSP and XG transputer are summarized in Table 1. Multiple-wire hit events are rejected prior to constructing those data products, so

the background rate is reduced in the products. The time history and the position histograms generated by the X-DSP are transferred to the XG transputer. The time history is used by the transient event detection trigger, while the position histograms are used to localize events detected by the trigger. The FREGATE time history is also transferred to the XG transputer and used for triggering. These data are transferred to the telemetry after reducing the time resolution by factors of 15 and 20 for time history and position histograms, respectively.

The triggering time scales implemented as of 2003 May are from 80 ms to 27 s, and the threshold levels are set to 4.7–8.0 sigma, depending on the time scale. To reduce the false trigger rate due to background variability, two background regions are taken before and after the foreground region and the expected background level in the foreground region is estimated by the linear interpolation. This method, however, introduces a localization delay which ranges from 5 s (trigger with 80 ms foreground) to 29 s (13 s foreground), depending on the triggering time scale. Thus, in the part of the orbit where the background rate is almost stable, one-sided triggers (which take background only before the foreground region) are used to reduce the delay time. The foreground time scales of the one-sided triggers are 5, 19 and 27 s. From the experience of recent in-orbit operation, the on-board localization delay time is found to be 5.5 s to 43 s, as summarized in table 4. Once a trigger is found, position histograms at the corresponding foreground and background region are extracted from the memory, and the localization procedure is applied to the data. When localization is completed, the trigger process continues to search for better time intervals based on the signal-to-noise ratio, and localization is performed for each updated foreground/background region. The localization is performed by the cross-correlation method. The cross-correlation score,  $C/\sigma_C$ , is calculated as:

$$C(j) = \psi_j [n \sum_i M_{ij} S_i - \sum_i S_i], \quad (1)$$

$$\sigma_{C(j)}^2 = \psi_j^2 [n^2 \sum_i M_{ij}^2 \sigma_{S_i}^2 + \sum_i \sigma_{S_i}^2], \quad (2)$$

where subscript  $i$  and  $j$  represent position and directional bins, respectively,  $\psi$  is the normalization constant,  $S$  is a background-subtracted observed histogram, and  $\sigma_S$  is the standard deviation of  $S$ .  $M$  is a “template”, a numerical simulation of the detector hit pattern for the corresponding direction. The burst direction is estimated by maximizing the cross-correlation score over possible directions.

### 3. Performance of the Proportional Counter

#### 3.1. Experiment

To calibrate the response of the proportional counter (PC), we irradiated a counter using characteristic X-rays of chlorine ( $K_\alpha = 2.6$  keV), titanium ( $K_\alpha = 4.5$  keV), iron ( $K_\alpha = 6.4$  keV), copper ( $K_\alpha = 8.0$  keV), and molybdenum ( $K_\alpha = 17.2$  keV) using an X-ray generator on the ground, and measured the positional and energy response. The X-rays were collimated to



**Table 1.** Data products generated by X-DSP and XG transputer.

Processor	Data type	Time resolution	Destination	Description
X-DSP	HK	4 s	Telemetry	House Keeping (HK) data of the instrument, such as power status, HV setting, temperatures of an electronics board and the support structure wall.
	TH	80 ms	XG Transputer	Time histories for 4 energy bands (approximately 2–5 keV, 5–10 keV, 10–17 keV and 17–25 keV) and for 4 counters.
	POS	330 ms	XG Transputer	Time-resolved position histograms for 2 energy bands (approximately 2–7 keV and 7–25 keV) and for 4 counters.
	PHA	4.9 s	Telemetry	Time-resolved energy spectrum for 4 energy bands (same as TH) and for 12 anode wires.
	TAG	256 $\mu$ s	Telemetry	Burst photon data tagged with time (8-bit), position (7-bit), energy (5-bit), and wire ID (4-bit). This data type is generated in the burst observation mode.
	RAW	1 $\mu$ s	Telemetry	2 words of unprocessed raw photon data from the instrument and 2 words of a time stamp. This data type is generated in the health check mode, 3 minutes per day.
Transputer	TH	1.2 s	Telemetry	This is made by rebinning the time histories received from the X-DSP.
	POS	6.6 s	Telemetry	This is made by rebinning the position histograms received from the X-DSP.
	Burst Information	Burst mode	Telemetry, VHF and Trigger Monitor on another node	Results of the trigger and localization processes are reported to the ground through S-band and VHF, and to the trigger monitor process for setting HETE-2 into the burst processing mode.

Note. The “destination” column represents where the data is transferred. “Telemetry” means that the data is transmitted to the ground over the S-band radio. TH and POS data are transferred to the XG transputer for further processing of burst detection and localization, then transmitted to the ground after reducing the time resolution.

0.2 mm diameter and irradiated at  $127 \times 54$  grid points with 0.94 mm spacing. The chlorine characteristic X-ray was obtained by putting a PVDC film of 20  $\mu\text{m}$  thickness in front of the Be window and irradiating it with titanium K X-rays, while the others were obtained directly from the primary targets. For more uniform and wider range of energy calibration, an experiment using a monochromator was also performed for the 6–26 keV energy range, with a 2 keV step. In these experiments, the bias voltage to the anode wire was changed from 1400 V to 1700 V to obtain the energy response for a wide range of gas gain.

After installing the WXM on the spacecraft, positional and energy calibration was performed by using  $^{55}\text{Fe}$  radioisotopes attached at the top of the support structure of the coded mask. The radioisotope is contained in a slit case and both sides of each counter are irradiated by two radioisotopes at 40 mm distance from the center of the counter. The detection count rate for each radioisotope is 1–2 c s $^{-1}$ .

### 3.2. Positional Response

We have measured a relation between the Position Measure,  $PM = L/(L + R)$  ( $L$ : pulse height measured at the left side of anode,  $R$ : pulse height at the right side), and the X-ray absorption position measured along the anode wire (figure 7). To derive the position measure at each position  $X$ , we stacked the data obtained by scanning perpendicularly across the anode wire at each fixed  $X$ -position, and calculated the median  $PM$ . The resulting relation deviates from linearity at both ends of the anode wire, mainly because of electric field distortion. The relation can be expressed by the following empirical formula to within 0.2 mm error:

$$\begin{aligned} X \text{ (mm)} &= a_1 + a_2 \times PM + \frac{a_3}{PM - a_4} - \Delta x & PM \geq a_0, \\ &= a_5 + a_6 \times PM + \frac{a_7}{PM - a_8} - \Delta x & PM < a_0, \end{aligned} \quad (3)$$

The coefficients  $a_0$ – $a_8$  were obtained independently for each anode. We noticed that the PM–X relation is gradually changing, as described in subsection 5.2, so these parameters are updated every six months based on in-flight calibration. The parameter  $\Delta x$  is a small correction term which is determined using the in-flight calibration. This systematic offset represents the effect of mechanical tolerance of the experimental alignment on the ground calibration.

Fig. 8 shows the positional resolution for Cu-K X-rays at each bias voltage. The primary purpose of the WXM is to localize GRBs with  $\sim 10'$  accuracy. This can be achieved with a positional accuracy of less than 1 mm for a 187 mm focal length, so the bias voltage should be greater than 1650 V. The positional resolution is mainly limited by Johnson noise, due to the relatively low resistivity of the carbon fiber. The positional resolution measured in this calibration experiment is expressed by the sum in quadrature of three components. The dominant component is due to electronic noise. The other contributions are statistical fluctuations of the center of electron clouds, and the finite X-ray beam size ( $\sim 0.2$  mm). Since the amplitude of the Johnson noise is inversely proportional to the square root of the resistance, it

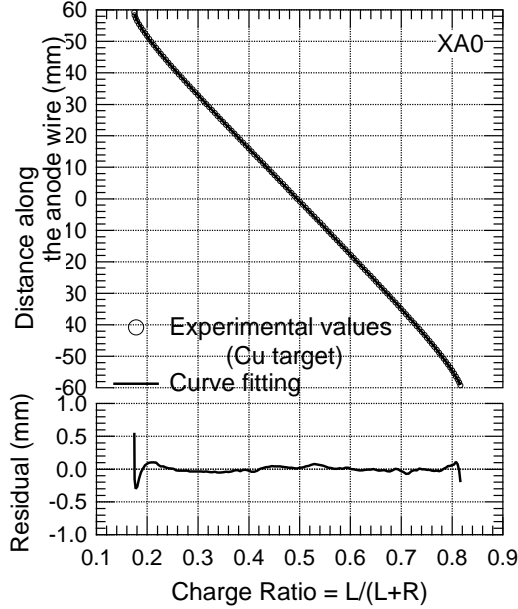


**Fig. 7.** Relation between the actual X-ray absorption position and the position measure defined by  $L/(L+R)$ , where  $L$  and  $R$  represent the pulse heights measured at the left and right sides, respectively.

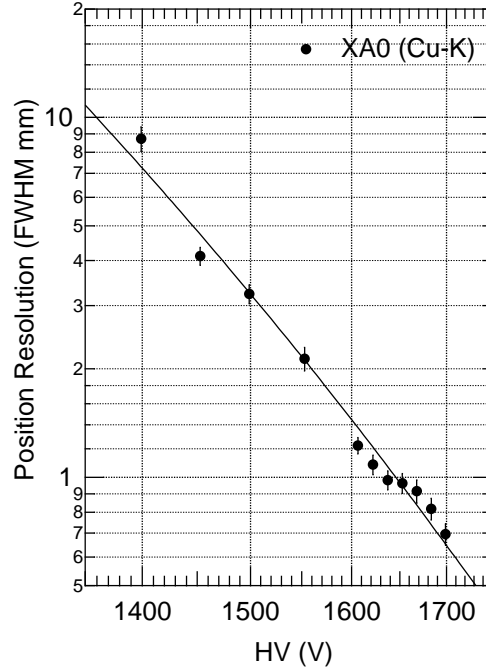


**Fig. 8.** Positional resolution vs. bias voltages for 8 keV X-rays.

is expected that the positional resolution is approximately a function of  $(L+R) \times \sqrt{R_i}$ .  $R_i$  is the resistance of the  $i$ -th anode wire, which ranges from 12.0 to 15.8 k $\Omega$ . As demonstrated in Shirasaki et al. (2000), the resolution can be well expressed as a function of the signal-to-noise ratio.

Since the direction of the electric field at the edges of the counter is not perpendicular to the direction of anode wire due to the internal structure, the X-position of gas amplification region systematically differs from that of X-ray absorption according to the three-dimensional absorption position. Thus, it is expected that the positional resolution is degraded at the counter edges. Figure 9 shows the error distributions at eleven X-positions (histograms) and positional resolution measured in FWHM (solid circles). They are obtained by accumulating calibration data at fixed X-positions of XA1 anode. The resolution is almost constant in the central region (from  $-40$  mm to  $+40$  mm), but it is substantially degraded as the position approaches the edge of the detector, due to the distortion of the electric field.

### 3.3. Energy Response

In figure 10, a 2-dimensional distribution of the average PH for the Cu-K X-ray ( $K_{\alpha} = 8.04$  keV) is shown together with the 1-dimensional projections at sections A-A', B-B', and C-C'. One can see that the gas gain increases at the left side, while it decreases at the right side. This is due to the internal mechanical structure of the PC.

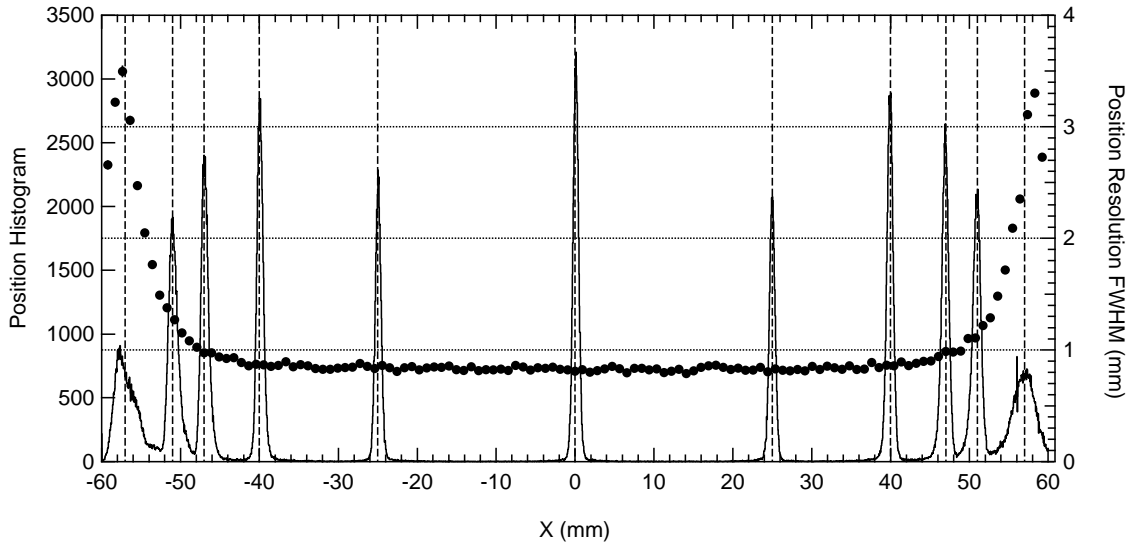


**Fig. 9.** Positional dependence of the position resolution. The histogram shows the position distribution for X-ray incidence at 11 X-positions shown with dashed lines, and the solid circles show the positional resolution measured in FWHM of the distribution.

In figure 11, the relations of the PH to the X-ray incident energy for various bias voltages (1300–1700 V) are shown for XA0 anode. The X-rays are irradiated at the position offset by 10 mm in the direction perpendicular to the wire. As shown in this figure, the PH is not linearly related to the energy at voltages above 1600 V, because of a self-induced space-charge effect. As mentioned in the previous section, we operate the PCs around 1650 V. We have therefore found it necessary to obtain a non-linear formula to translate PH to energy. The experimental result is well represented by the following formula:

$$E = a \cdot (\text{PH}/c) + b \cdot \sinh(\text{PH}/c) + d \cdot (\text{PH}/c)^2 \quad (4)$$

We assume that the relation depends only on gas gain and parameterize the coefficients  $a$ ,  $b$ ,  $c$ , and  $d$  as a function of bias voltage  $v$  for the case of reference anode XA0. The gas gain is slightly different for each anode because of the difference in the wire radius and electric field, so the equivalent potential  $v$  of the above formula is separately determined for each anode. The spatial non-uniformity of the gas gain is corrected by introducing a spatial dependence to  $v$ .

Using the PH-energy relation formula obtained above, the energy resolution is determined for energies of 6–24 keV and for bias voltages of 1400–1700 V. In figure 12 the results for off-wire incidence are plotted against energy. However, at a low bias voltage of 1400 V, energy dependence of the resolution satisfies the  $1/\sqrt{E}$  law; at higher voltages it no longer follows the law, owing to the space-charge effect. We find that the resolution is well expressed as a function of the empirical parameter  $M^{0.23} \times n_0$  for various bias voltages. Details are described in Shirasaki et al. (2000).

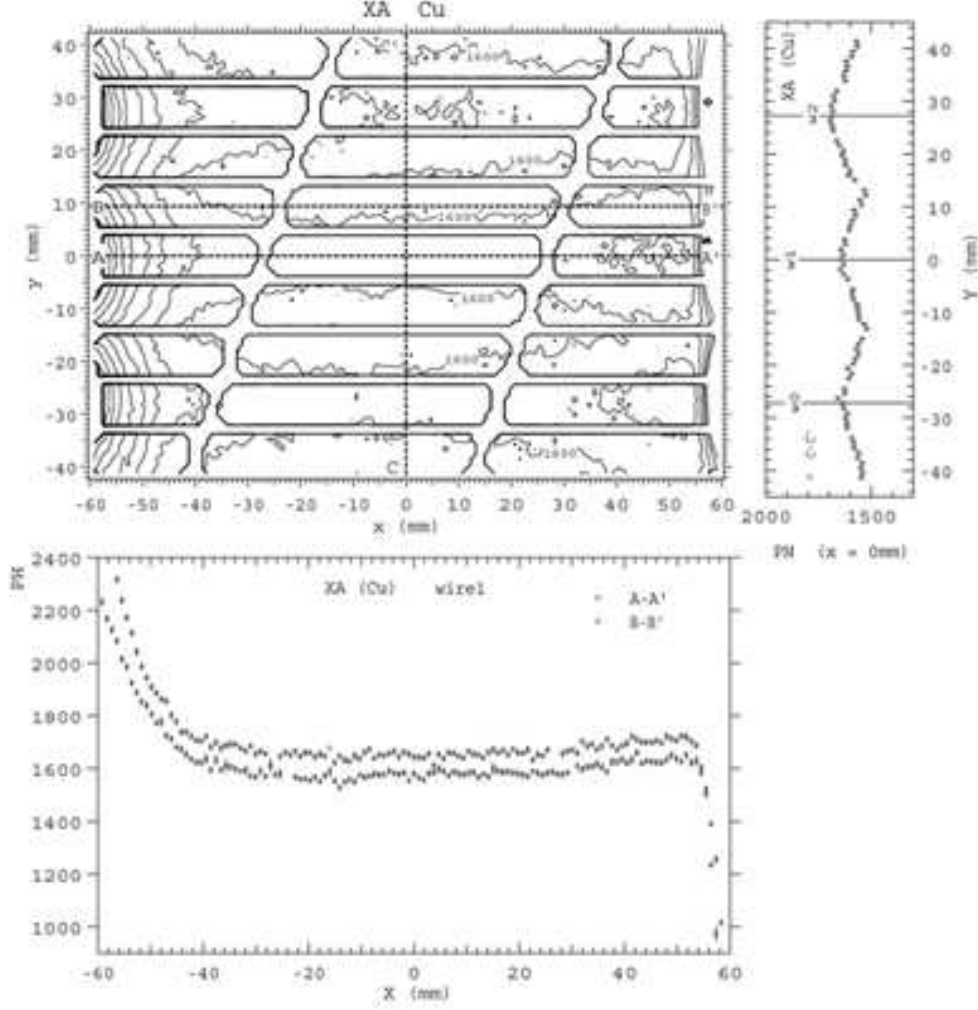


**Fig. 10.** Gain uniformity of the XA detector at Cu K energy. The left-top panel shows a contour plot of the gain distribution, the bottom panel shows the gain distribution along the line of A–A' and B–B', and right panel shows the gain distribution along the line of C–C'.

#### 4. RIKEN Ground Localization Method

A ground analysis of the GRB localization by the WXM is performed by two independent methods, the Chicago Bayesian method (Graziani et al. 2003) and RIKEN cross-correlation method (Shirasaki et al. 2003a). The RIKEN localization method is based on the variance-weighted cross correlation method, which searches for the direction where the simulated position histogram best matches the observed one. The procedure consists of two parts. First we determine a coarse location  $(\theta_{x,0}, \theta_{y,0})$  using the model histograms simulated for the directions spaced by  $0^\circ.2$  along  $\theta_x = 0$  and  $\theta_y = 0$  axes. Next the fine location is determined using models simulated along  $\theta_x = \theta_{x,0}$  and  $\theta_y = \theta_{y,0}$  by every  $0^\circ.05$  step. In the model calculation, we take into account the following effects: (1) the slant penetration effect, (2) positional resolution,

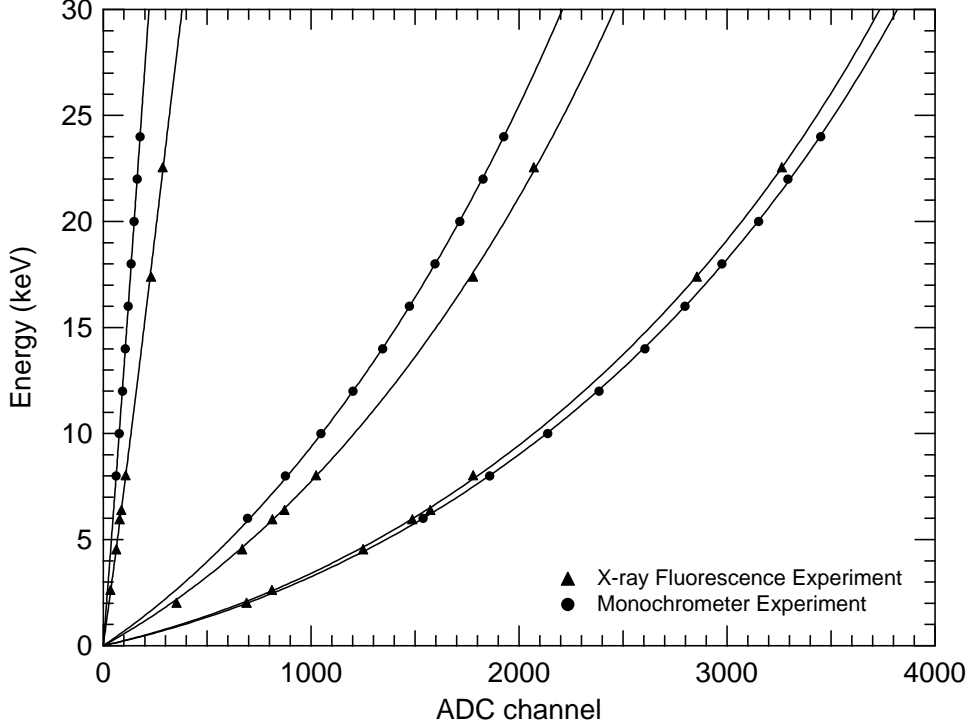


**Fig. 11.** X-ray incident energy vs. measured pulse height. The solid circles show the experimental data and the lines show the result of parameterization using equation (4), the coefficients of which were derived as a function of equivalent bias voltage parameter  $v$ . From left to right, the curves correspond to voltages  $v = 1299, 1361, 1599, 1618, 1694, 1699$  V, respectively.

$\sigma(E, x)$ , as a function of energy and X-ray absorption position, (3) obscuration function,  $f(x)$ , by the PC body structure, the side wall, and the coded mask. The model histogram for an X-ray of energy  $E$  is expressed as

$$\begin{aligned}
 P(x, E) = & \epsilon(E) \cdot \frac{1}{\sqrt{2\pi}\sigma(E, x')} \cdot \frac{1}{\lambda_x(E)} \int_{x_{\min}}^{x_{\max}} dx'' f(x''), \\
 & \times \int_{x''}^{x''+d\tan(\theta_x)} dx' e^{-\frac{(x-x')^2}{2\sigma^2(E, x')}} e^{-\frac{(x'-x'')}{\lambda_x(E)}}, \quad (5)
 \end{aligned}$$

where  $\epsilon$  is the transmission coefficient of the  $100 \mu\text{m}$  Be window and the  $7.62 \mu\text{m}$  thermal shield,  $\lambda_x$  is the projection of the mean free path onto the wire direction,  $x_{\min}$  and  $x_{\max}$  are the available range of anode wire, which is from  $-57$  mm to  $+57$  mm, and  $d$  is the depth of an anode cell. Denoting the source spectrum by  $F(E)$ , the spectrum-weighted model histogram is given by

$$M(x) = \int F(E) P(x, E). \quad (6)$$

We usually assume an  $E^{-1.5}$  spectrum for a GRB analysis. For the purpose of WXM astrometric calibration, we use an appropriate spectrum type for each X-ray source. The cross-correlation score is calculated by equations (1) and (2). The score is evaluated at every  $0^\circ.05$ , and the

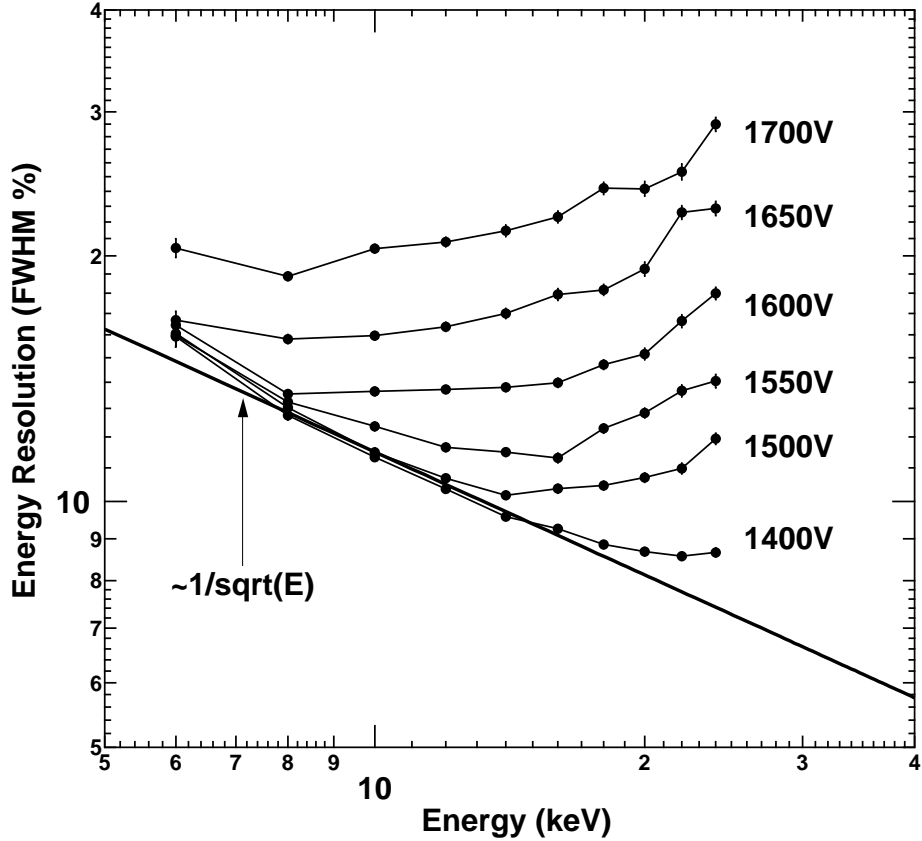


**Fig. 12.** Energy resolution at energies from 6 to 24 keV for bias voltages from 1400 to 1700 V

maximum value is obtained with  $0^{\circ}.01$  accuracy by interpolation.

The localization error is estimated by simulating 1000 sets of position histograms based on the observational data. The simulation is performed by introducing a Poisson fluctuation to the observed position histograms for the foreground and background regions, and applying the same localization procedure as that applied to the observational data. A 90% C.L. error circle and the 90% C.L. rectangle are then calculated by requiring that 90% of the simulated locations are contained in the error region. We choose a circle or rectangle depending on which of the two regions subtends the smallest solid angle. The rectangular regions are usually preferable when the signal-to-noise ratio in one detector is significantly smaller than in the other, e.g. when a GRB occurs at the edge of the FOV in the X direction but not in the Y direction.

## 5. In-Orbit Performance of the WXM

### 5.1. Background

The WXM background consists of a non-X-ray background (NXB; charged particles) which dominates in a restricted region of the HETE-2 orbit, the cosmic X-ray background

(CXB) which dominates over the majority of the orbit, and the steady X-ray point source background from sources such as the Crab Nebula and Sco X-1. To reduce the NXB, the anti-coincidence method is used. In laboratory calibration, the total background count rate was measured as  $30 \text{ c s}^{-1}$  for one counter, and after the anti-coincidence and energy selection the background rate was reduced to  $4.4 \text{ c s}^{-1}$  in the energy range 2–25 keV, which corresponds to  $4.7 \times 10^{-4} \text{ c s}^{-1} \text{ cm}^{-2} \text{ keV}^{-1}$ .

The background count rate in orbit is mostly dependent on the geographic coordinates of the spacecraft. The total count rate and anti-coincidence rate for the 2–25 keV energy range are shown in figure 13 as a function of the geographic coordinates. According to the background level and its time variability, the HETE-2 orbit is divided into 4 types of geographic regions:

1. The most quiet region of longitude from  $10^\circ\text{W}$  to  $120^\circ\text{E}$  over the African Continent, the Indian Ocean, and the Oceanian region, where the total count rate is very stable and as low as  $1000 \text{ c s}^{-1}$ . In this region, the 2–25 keV event rate with anticoincidence is  $530 \text{ c s}^{-1}$ , while the event rate without anticoincidence is  $560 \text{ c s}^{-1}$ .
2. The moderate background region from  $120^\circ\text{E}$  to  $105^\circ\text{W}$  over the Pacific Ocean, where the total count rate is a time variable in the range  $1000\text{--}1500 \text{ c s}^{-1}$ .
3. The pre-SAA region from  $105^\circ\text{W}$  to  $60^\circ\text{W}$  over the East Pacific Ocean and the Republic of Colombia, where the total count rate is usually the same as that of region 2, but can drastically increase at times of strong solar activity.
4. The SAA region from  $60^\circ\text{W}$  to  $10^\circ\text{W}$  over Brazil and the West Atlantic Ocean, where the count rate exceeds  $5000 \text{ c s}^{-1}$ .

By applying the anti-coincidence condition, the proton background in the SAA region is effectively reduced by more than 90%, but the transient events in the pre-SAA region are not effectively rejected. This is because the transient events mostly consist of electrons and/or positrons which have a shorter mean free path in the proportional counter than the dimensions of an anode cell, so they are absorbed in a single cell.

The measured counting rates for 2–25 keV anti-coincidence events due to the Crab Nebula and Sco X-1 are  $270 \text{ c s}^{-1}$  and  $2040 \text{ c s}^{-1}$ , respectively, when they are at the on-axis direction.

In figure 14, the probability distribution of the background rate in 2001 October is shown for 2–25 keV anti-coincidence events. The mode of the background rate is  $\sim 530$  and in 96% of the WXM on-time the background rate is less than  $640 \text{ c s}^{-1}$ . Assuming a GRB of 10 s duration and a background rate of  $530 \text{ c s}^{-1}$ , the 5-sigma trigger threshold corresponds to 0.13 Crab.

### 5.2. *In-Orbit Calibration of Positional Response*

From long-term monitoring of the signal produced by the radioisotopes, we noticed that the apparent position calculated by equation (3) is gradually changing at a rate of 1 mm per



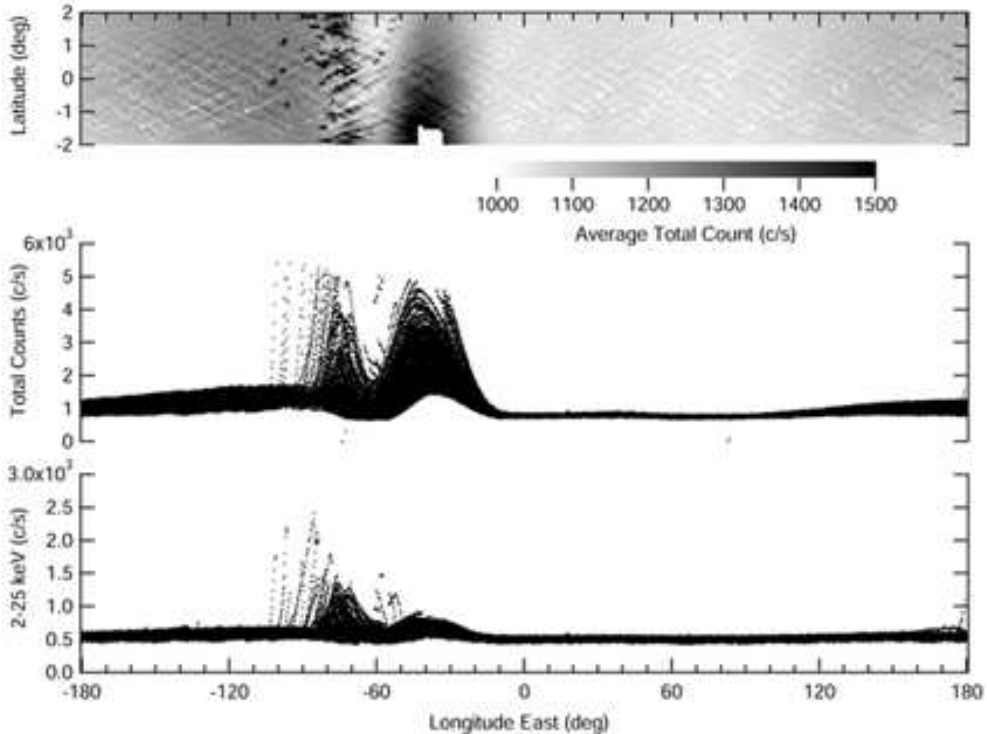


**Fig. 13.** Background counting rate in the HETE orbit. The top panel shows the averaged total counting rate at latitude from  $-2^\circ$  to  $+2^\circ$ . The blank at the center of SAA region is due to lack of observations at that longitude. The middle panel shows a typical total count rate distribution in one month. The bottom panel shows a typical count rate distribution of anti-coincidence events of 2–25 keV in one month.

3 years at the position irradiated by the calibration sources. The variation of the position measured for XA1 is shown in figure 15. The cause of this variation is not understood yet, but is likely due to a change in the metallic contact of the carbon wire. In order to correct this variation, we assumed that the correction is linear in the position measure.

After the launch of the spacecraft, we performed a consistency check of the positional response among all of the anodes by localizing Sco X-1 using each individual anode. The average difference for each anode is summarized in table 2. The corresponding positional offset defined in equation (3) is also listed there. We interpret these systematic errors as the effect of the mechanical tolerance of the experimental alignment on the ground calibration. We correct them by subtracting the offset in the equation (3).

Modeling the positional response, we simulated a mask pattern measured by the WXM, and compared it with the observed Crab Nebula image. The result is shown in figure 16. The simulated Crab Nebula images are in good agreement with the observed images.

### 5.3. In-Orbit Gain and Spectrum Calibration

In figure 17, long-term gas gain variations monitored using the radioisotopes are shown for the XA1, XB1, YA1, and YB1 anodes. For the XA and XB counters, the gas gain gradu-

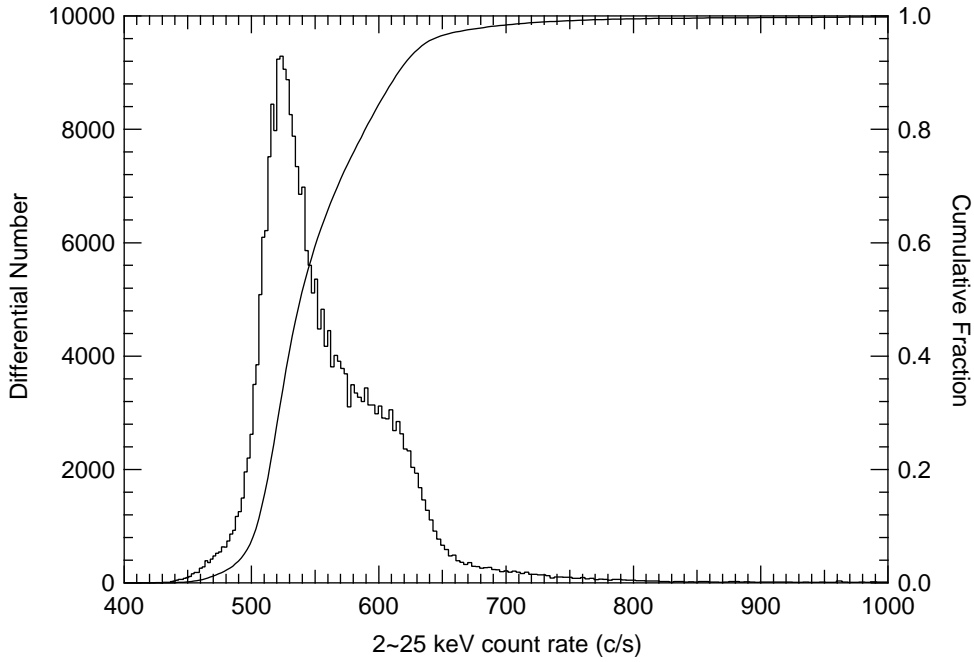


**Fig. 14.** Background count rate distribution at the 2–25 keV energy range. The histogram shows the differential distribution and the solid line shows the cumulative distribution.

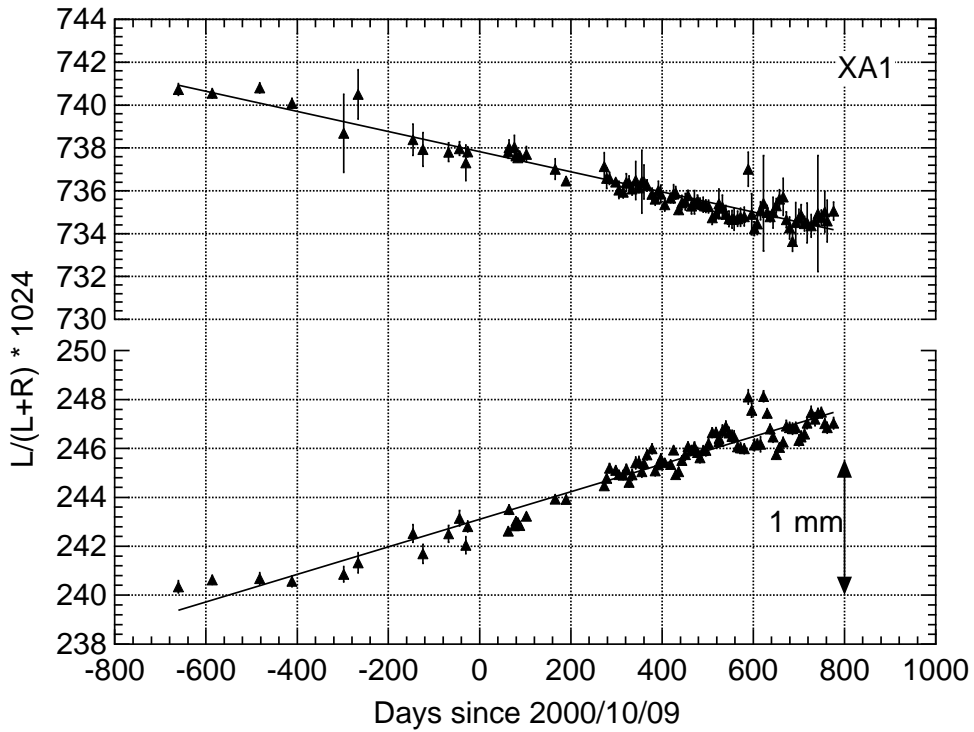


**Fig. 15.** Long-term variation of the position measures of the calibration sources for the case of an XA0 wire. Day 0 corresponds to the HETE-2 launch date.

**Table 2.** Systematic difference of the calculated directions of Sco X-1.

	$\langle\Delta\theta\rangle$	$\sigma$	$N$	$\Delta x$		$\langle\Delta\theta\rangle$	$\sigma$	$N$	$\Delta x$
	(deg)	(deg)		(mm)		(deg)	(deg)		(mm)
XA0	-0.010	0.028	43	0.034	YA0	-0.033	0.022	29	0.108
XA1					YA1				
XA2	0.066	0.025	41	-0.216	YA2	0.051	0.014	33	-0.167
XB0	-0.072	0.024	40	0.235	YB0	-0.071	0.017	25	0.232
XB1	-0.016	0.019	44	0.052	YB1	-0.049	0.018	21	0.160
XB2	0.002	0.035	40	-0.005	YB2	0.004	0.012	20	-0.012

Note.  $\langle\Delta\theta\rangle$ , average difference from the direction obtained for reference anodes XA1 or YA1;  $\sigma$ , standard deviation of the difference from the average;  $N$ , number of samples used for this analysis;  $\Delta x$ , corresponding offset parameter of equation (3).

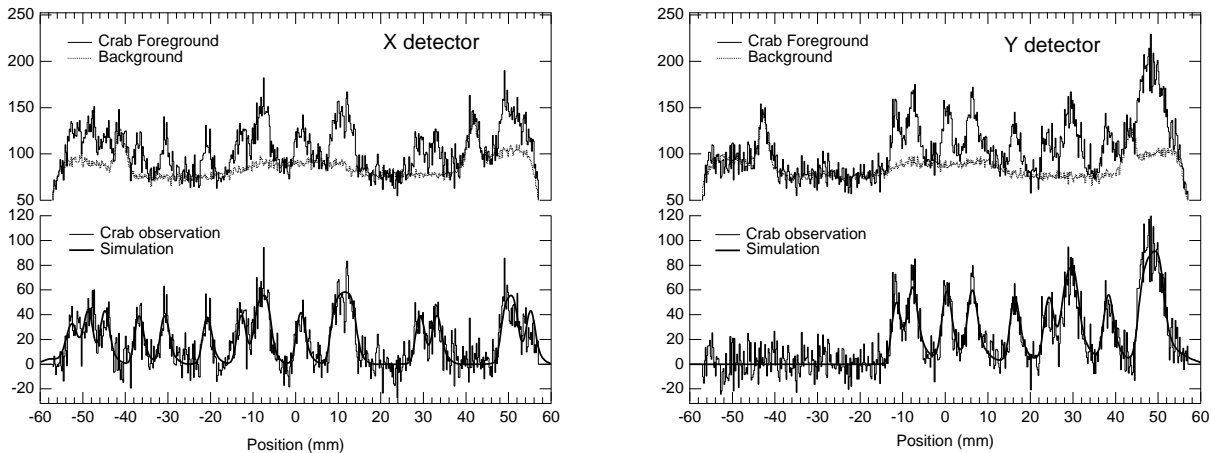


**Fig. 16.** Crab Nebula images taken by the WXM. Each top panel shows position histograms of the photons observed during the period when Crab is in the FOV (solid line) and outside the FOV (dotted line). Each bottom panel shows a comparison of background-subtracted Crab Nebula images (histogram) and simulated images (thick line). The two peaks in the background histogram around  $\pm 40$  mm are due to the on-board calibration isotopes.

ally increased until day 200 since the launch date, and decreased thereafter. For the YA and YB counters, the gas gain was still continuing to increase at day 800. The calibration experiment was carried out at around day  $-700$ , so the maximum gain deviation from the ground experiment is about 2% as of day 800.

The methods for calibrating the WXM energy response are limited to the observations of Crab Nebula and monitoring the radioisotope signal, since no other sufficiently bright celestial X-ray source is ever in the WXM FOV, with the exception of Sco X-1. Because Sco X-1 is a strongly variable source, it is not suitable for an energy calibration. Using the Crab Nebula and the signal from the radioisotopes, we may calibrate the temporal gain variation, the absolute gain scale, and the detector efficiency. The detector efficiency and gain scale are checked using

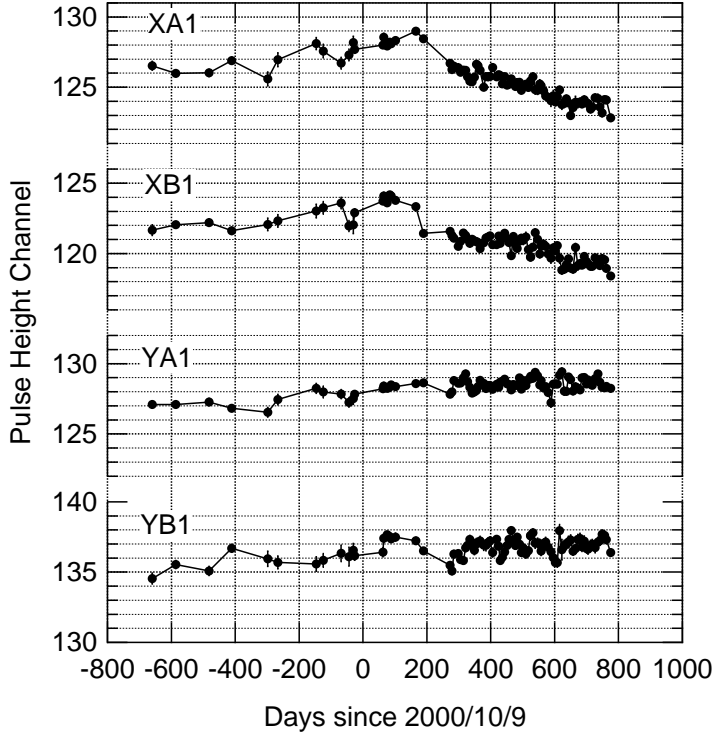


**Fig. 17.** Long-term gas gain variations monitored using the radioisotopes. From the top, XA1, XB1, YA1, and YB1. Day 0 corresponds to the HETE-2 launch date.

Crab Nebula observations, and the temporal gain variation is corrected by monitoring the gain using the signal from the radioisotopes, as described above. The other items not calibrated in-orbit, such as the energy resolution, the spatial gain variation, and the energy pulse height linearity, rely on the ground calibration experiment.

To investigate the detector efficiency below 3 keV, we performed observations of the Crab Nebula while operating at a low bias voltage (1400 V). At this setting, the pulse height and energy relation shows better linearity than at the standard setting, so we can check the detector efficiency without being affected by uncertainty of their non-linear relation at energies below 3 keV, where absorption by a Be film is significant. The location of the Crab Nebula in instrument coordinates during the observation period was  $\theta_x = 21^\circ.6$  and  $\theta_y = 12^\circ.7$ . Only the YB detector was calibrated by this observation. In figure 18, the observed Crab Nebula spectrum is compared with a simulated spectrum of power-law index 2.1 and absorption column density  $3 \times 10^{21} \text{ cm}^{-2}$ , which is a canonical Crab spectrum. The absolute gain scale at 1400 V is determined by scaling down of the effective bias voltage parameter for the standard HV setting so as to reproduce the ground calibration data taken by  $^{55}\text{Fe}$  radioisotopes. The reduced  $\chi^2$  of the comparison between the observed and simulated spectra is 1.03 (d.o.f. = 118). From this result the accuracy of the detector efficiency at energies below  $\sim 4$  keV is expected to be better than 10%.

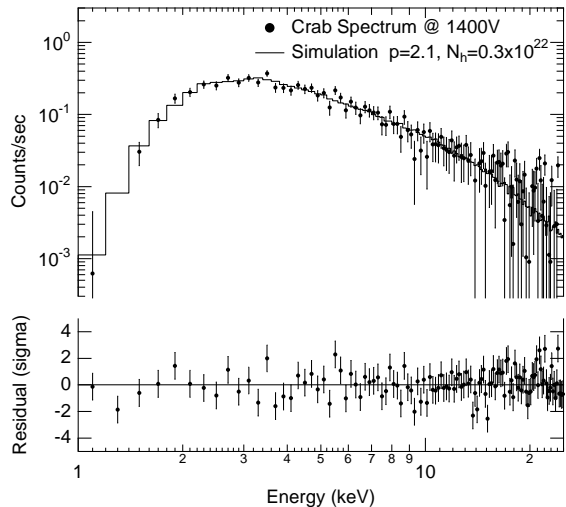


**Fig. 18.** Comparison of the observed Crab Nebula spectrum with the simulated spectrum assuming a power-law with index 2.1 and  $3 \times 10^{21} \text{ cm}^{-2}$  of absorption column density. The observation is performed at a bias voltage of 1400 V.

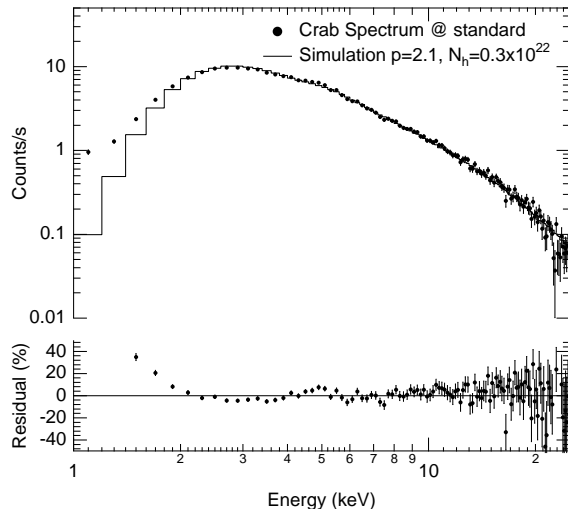


**Fig. 19.** Same as figure 18, but for standard HV setting.

Next, we present the result of Crab Nebula observations carried out at the standard setting, that is 1668 V for XA and YB, and 1653 V for XB and YA. The gain scale is determined by adjusting the gain parameters so as to reproduce the canonical Crab Nebula spectrum for each wire. The measured energies of the calibration sources are checked to be accurate within 2%. In figure 19, the observed Crab Nebula spectrum is compared with the simulated spectrum. Above 2 keV, the reduced  $\chi^2$  between the two spectra is 1.79 (d.o.f. = 114), so they are statistically inconsistent with each other. The most significant inconsistency is the spectrum around 5 keV, where the observed spectrum is 5% higher than the Monte Carlo simulation. The cause of this inconsistency is under investigation. Below 2 keV, the observed count rates are higher than the expected ones. This is probably due to the inaccuracy in the energy-pulse height relation, and/or energy resolution at energies below 2 keV, where we have no calibration data.

Spectrum fitting for Crab Nebula observations was performed for various incidence angles (Shirasaki et al. 2003b). From this result, the systematic uncertainty of the power-law index, absorption column density, and absolute flux are estimated to be  $\pm 0.1$ ,  $\pm 0.2 \times 10^{22} \text{ cm}^{-2}$  and  $\pm 10\%$ , respectively.

#### 5.4. WXM Alignment Calibration

To calibrate the alignment between the WXM optical axis and the spacecraft Z-axis, we used observations of the Crab Nebula and of Sco X-1. The observation periods of the Crab

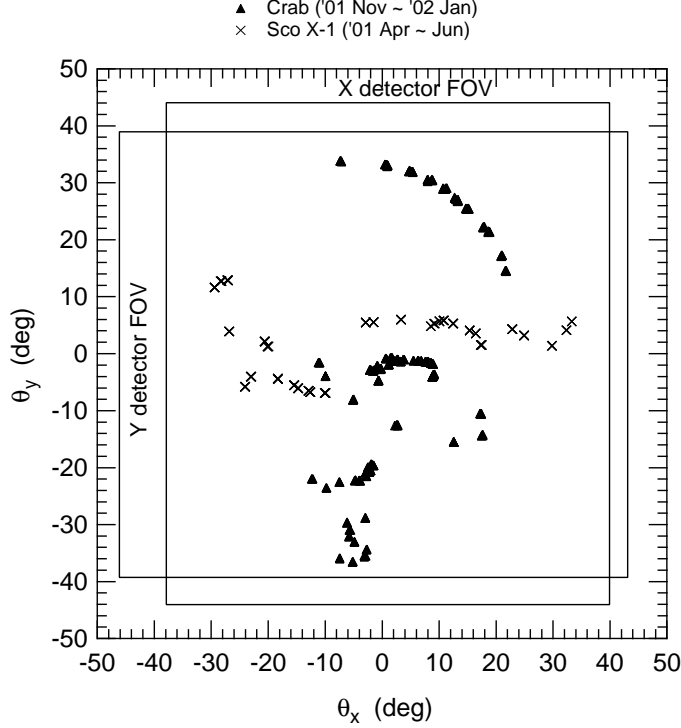


**Fig. 20.** Locations of Crab and Sco X-1 during the WXM alignment calibration.

Nebula and Sco X-1 are given in table 3. The source locations in the WXM field of view are plotted in figure 20. These observations were made in the quiet background region of the HETE-2 orbit. The region of  $\theta_x = -30^\circ$  to  $33^\circ$  and  $\theta_y = -37^\circ$  to  $34^\circ$  are calibrated by these observations.

The data were divided into 20 s and 50 s subsets for Sco X-1 and Crab Nebula data, respectively, and the localization procedure was applied to each subset. The data type used in this analysis was RAW. The charge ratio (PM) correction derived in subsection 5.2 was applied as a function of UT. The binning size of the position histograms was 0.2 mm. The background was obtained from the data taken in the quiet background orbital region, during periods when Crab Nebula and Sco X-1 were out of the field of view. The source locations in the WXM coordinate system were calculated by the cross-correlation method, as described in section 4. In simulating the position histogram used for taking a cross-correlation with the observed data, a power-law energy spectrum of power index 2.1 was assumed for the Crab Nebula and a 6 keV thermal bremsstrahlung spectrum was assumed for Sco X-1.

The calculated directions in WXM coordinates were translated to the spacecraft coordinates system using the rotation matrix, defined as

$$V_{SC} = R_x(a) \cdot R_y(b) \cdot R_z(c) \cdot V_{WXM}, \quad (7)$$

where  $V_{WXM}$  is the unit vector describing the source location in WXM coordinates,  $V_{SC}$  is the unit vector describing the source location in spacecraft coordinates,  $R_x(a)$  is a rotation matrix with respect of the  $x$ -axis, and so on. The location in celestial coordinates was obtained by

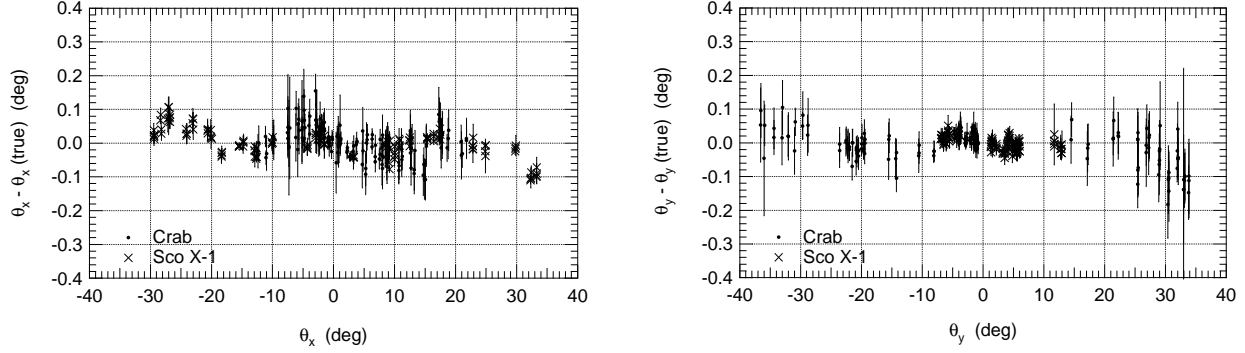


**Fig. 21.** Localization errors plotted against the source direction  $\theta_x$  and  $\theta_y$ .

**Table 3.** Observational periods of Crab Nebula and Sco X-1 for the purpose of alignment calibration.

Source	Number of samples	Period
Crab	437	2001 Nov. 08 – 2002 Jan. 19
Sco X-1	208	2001 Apr. 23 – 2001 Jun. 30

using the spacecraft aspect data, expressed as the direction of the spacecraft Z-axis in celestial coordinates and the roll angle about the Z axis. The precision of the spacecraft aspect used in this analysis was typically 1 arcmin. The Euler angles ( $a$ ,  $b$  and  $c$ ) were determined by least-squares minimization of the difference between the calculated locations and the actual source locations. We defined  $\chi^2$  as

$$\chi^2 = \sum \left\{ \frac{(\theta_{x,i}^{\text{cal}} - \theta_{x,i}^{\text{src}})^2}{\sigma_{x,i}^2} + \frac{(\theta_{y,i}^{\text{cal}} - \theta_{y,i}^{\text{src}})^2}{\sigma_{y,i}^2} \right\}, \quad (8)$$

where  $\theta_{x,i}^{\text{cal}}$  and  $\theta_{y,i}^{\text{cal}}$  are the  $x$  and  $y$  components of the calculated location for the  $i$ -th sample,  $\theta_{x,i}^{\text{src}}$  and  $\theta_{y,i}^{\text{src}}$  are the actual source location derived from the spacecraft aspect data and assumed Euler angles, and  $\sigma_{x,i}^2$  and  $\sigma_{y,i}^2$  are statistical localization errors for their respective components. The obtained rotation angles are  $a = 0^\circ.18$ ,  $b = 0^\circ.34$  and  $c = 0^\circ.07$ . The r.m.s. of the localization error of Sco X-1 is reduced from  $20.0'$  to  $2.8'$  by the alignment correction, and the r.m.s. for the Crab Nebula is  $4.3'$  after the correction.

In figure 21 the localization error of  $\theta_x$  and  $\theta_y$  are plotted against  $\theta_x$  and  $\theta_y$ , respectively. The errors of the directions are less than  $0^\circ.1$  at any calibration region and no significant directional dependence is seen. The overall systematic error is estimated by requiring that the reduced  $\chi^2$  be unity by adding an additional error term in quadrature to the statistical error. The resulting systematic error is  $1'.83 \pm 0'.14$ , to be added in quadrature to the statistical error in each of the  $\theta_x$  and  $\theta_y$  directions.

We have investigated the accuracy of the estimated localization error radius using the XRB and SGR events, whose coordinate are known to better precision than the WXM localization precision. The error is uniform in the location in the FOV, and no significant systematic

deviation from the true location is seen for any direction. The error distribution of XRBs follows the expected distribution, confirming that the error radius is correctly estimated. More details are described in Shirasaki et al. (2003b).

### 5.5. Performance of In-Orbit GRB Localization and Operational Efficiency

The accuracy of the flight localization can be inferred from the total cross-correlation score, i.e. imaging SNR defined by  $\sqrt{\text{IMAGE\_SN\_X}^2 + \text{IMAGE\_SN\_Y}^2}$ , where  $\text{IMAGE\_SN\_X}, \text{IMAGE\_SN\_Y}$  represent the cross-correlation score corresponding to the X and Y directions, respectively. In order to determine a threshold criterion for automatically sending out WXM localizations to the GRB Coordinates Network (GCN), we examined the localization accuracy as a function of the imaging SNR. Figure 22 shows the number of correct localizations of XRBs (good localization with location error less than  $0^\circ.5$ ) for which the imaging SNR exceeds a given threshold value, and also shows the the number of good localizations minus the number of bad localizations (localization error larger than  $0^\circ.5$ ). The criteria for sending to the GCN should be determined so that the false alert rate is minimized while the number of correct localizations is maximized. As a compromise between the two requirements, we chose a threshold of the imaging SNR such that the difference between the number of good and bad localization is maximal. From figure 22, the threshold is 3.7.

In order to estimate the sensitivity of the flight localization algorithm to the total fluence of a GRB, we carried out a Monte Carlo simulation of GRB events, and applied the flight localization procedure to the simulated data. In the simulation, we assumed an energy spectrum of  $E^{-1.5}$ , a uniform directional distribution in the WXM FOV, a 10 s duration with a constant flux, and a background rate of  $530 \text{ c s}^{-1}$ . The correct localization rate for the GRB locations in the range  $\theta_{x,y} = -30^\circ$  to  $30^\circ$  (solid triangles) and the fraction of correct localizations to be sent to the GCN (solid circles) are shown in figure 23 as a function of the total fluence. From this result, one can see that the flight localization sensitivity is  $> 10^{-7} \text{ erg cm}^{-2}$ , and that the false alert rate is 50% for GRB with  $10^{-7} \text{ erg cm}^{-2}$ , reaches maximum at  $3 \times 10^{-7} \text{ erg cm}^{-2}$ , and decreases above that fluence. The reason for the increase in the false alert rate above  $3 \times 10^{-7} \text{ erg cm}^{-2}$  is that GRB with locations at the edge of the FOV ( $|\theta_{x,y}| > 30^\circ$ ) are incorrectly localized to the region  $|\theta_{x,y}| < 30^\circ$  and produce imaging SNR larger than 3.7.

Using  $\sim 80$  XRBs, we checked the statistics of the propagation times of burst locations determined by the flight software (Shirasaki et al. 2003c). The result shows that 30% of the events are propagated to the ground in 60 s, 50% in 150 s, and 90% in 590 s. The size of the localization error depends on the fluence and the position of GRB in the FOV. The typical total error ranges from 4 arcmin to 40 arcmin in diameter.

WXM operations are performed on the night side of the HETE-2 orbit. Operations are extended by several minutes beyond the terminators during moderate solar activity, in order to enhance the GRB detection probability. When the solar activity is high and X-class flares are



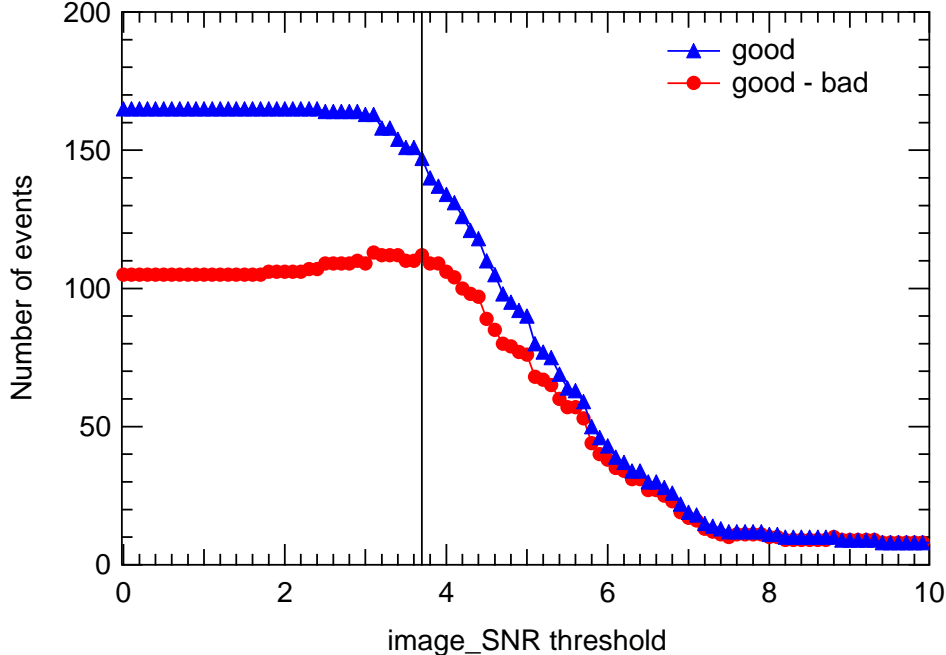


**Fig. 22.** Number of events localized to known X-ray sources with an error less than  $0^\circ.5$  (good events) are shown with triangles as a function of the threshold of imaging SNR, where imaging SNR is defined by a square root of sum in quadrature of image SNRs for X and Y directions. The differences between the number of good events and bad events (error larger than or equal to  $0^\circ.5$ ) are shown with solid circles.

likely, operations are reduced to the dusk-to-dawn portion of the orbit, so as to avoid any risk of direct irradiation by a strong solar flare in the event that a loss of the spacecraft attitude control should result in WXM pointing toward the Sun. The monthly operational efficiency is shown in figure 24, together with the cumulative number of localized GRBs. On-time has been quite stable at a level of 40%–50% since 2001 September. A total of 38 GRBs have been localized by the WXM as of 2003 May 1. As seen in figure 24, the localization rate increased around 2002 August, mainly due to improvements in operational practice (principally head-nodding of the spacecraft to avoid the moon and bright X-ray sources). The current estimated GRB localization rate is 28 per year, using observations from 2002 August until 2003 April.

In table 4, a summary of the localized GRBs, the delay time for reporting their locations, dimensions of the error region quoted in the first and last GCN notice/circular, and the approximate fluence of the GRB are presented. Six real-time localizations were obtained and propagated in times ranging from 22 s to 9 min from the onset of the bursts. The typical delay time of the ground localization reports are 1 to 3 hr. The minimum fluence of the localized GRBs is  $1 \times 10^{-7}$  erg  $\text{cm}^{-2}$  in 2–25 keV.

**Table 4.** Summary of the localized GRBs.

	Reported time	On board delay	Error size	Refined er- ror size	Fluence (2–25 keV) (erg cm <sup>-2</sup> )	Comment
GRB 010213	36h14m		60′ dia.		$7 \times 10^{-7}$	ground trigger
GRB 010326B	4h45m		36′ dia.		$1 \times 10^{-7}$	
GRB 010612	69h19m		72′ dia.		$5 \times 10^{-7}$	Sco X-1 in the FOV
GRB 010613	56h55m		72′ dia.		$6 \times 10^{-6}$	Sco X-1 in the FOV
GRB 010629	8h57m		30′ dia.		$2 \times 10^{-6}$	Sco X-1 in the FOV
GRB 010921	5h10m		20′ × 10°		$1 \times 10^{-5}$	1-D localization, OT
GRB 010928	6h10m		12′ × 10°		$2 \times 10^{-6}$	1-D localization
GRB 011019	12h07m		70′ dia.		$4 \times 10^{-7}$	ground trigger
GRB 011130	4h33m		120′ dia.	15.2′ dia.	$6 \times 10^{-7}$	
GRB 011212	8h20m		22′ dia.		$5 \times 10^{-7}$	ground trigger
GRB 020124	1h26m		27′ × 35′	24′ dia.	$2 \times 10^{-6}$	OT
GRB 020127	1h46m		24′ dia.	16′ dia.	$6 \times 10^{-7}$	
GRB 020305	9h56m		50′ dia.		(*1)	OT
GRB 020317	52m36s		60′ dia.	36′ dia.	$1 \times 10^{-7}$	
GRB 020331	40m22s		20′ dia.	16′ dia.	$1 \times 10^{-6}$	OT
GRB 020531	1h28m		120′ dia.	43′ × 64′	$1 \times 10^{-7}$	
GRB 020625	2h54m		18′ × 32′	18′ × 32′	$2 \times 10^{-7}$	
GRB 020801	1h56m		11′ × 13°	9′ × 26′	$6 \times 10^{-6}$	
GRB 020812	9m04s	32 s	60′ dia.	10′ × 25′	$5 \times 10^{-7}$	real time alert
GRB 020813	4m13s	43 s	28′ dia.	8′ dia.	$1 \times 10^{-5}$	real time alert, OT
GRB 020819	1h38m		14′ dia.		$2 \times 10^{-6}$	
GRB 020903	3h51m		33′ dia.		$1 \times 10^{-7}$	
GRB 021004	48s	20 s	60′ dia.	20′ dia.	$5 \times 10^{-7}$	real time alert, OT
GRB 021016	1h44m		19′ × 6°	15′ × 11°	$3 \times 10^{-6}$	1-D localization
GRB 021021	16h15m		40′ dia.		$1 \times 10^{-7}$	ground trigger
GRB 021104	2h46m		25′ × 42′		$4 \times 10^{-7}$	
GRB 021112	1h21m		54′ dia.	40′ dia.	$2 \times 10^{-7}$	
GRB 021113	2h01m		14′ × 29′	9′ × 26′	$1 \times 10^{-6}$	
GRB 021211	22s	5.5 s	28′ dia.	10′ dia.	$1 \times 10^{-6}$	real time alert, OT
GRB 030115	1h11m		20′ dia.		$8 \times 10^{-7}$	OT
GRB 030226	1h49m		30′ dia.		$2 \times 10^{-6}$	ground trigger, OT
GRB 030323	4h58m		36′ dia.		$4 \times 10^{-7}$	OT
GRB 030324	24.2s	19 s	28′ dia.	14′ dia.	$5 \times 10^{-7}$	real time alert
GRB 030328	2h01m		9′ dia.		$4 \times 10^{-5}$	OT
GRB 030329	(*2)		(*2)	2612′ × 2.25°	$5 \times 10^{-5}$	1-D localization, OT
GRB 030416	15h44m		14′ dia.		$1 \times 10^{-6}$	ground trigger
GRB 030418	3m35s	31 s	28′ dia.	18′ dia.	$2 \times 10^{-6}$	real time alert, OT
GRB 030429	1h52m		10′ × 20′		$8 \times 10^{-7}$	OT

Note. Given are delay time for reporting the WXM location, delay time of the on-board location relative to the GRB onset time,

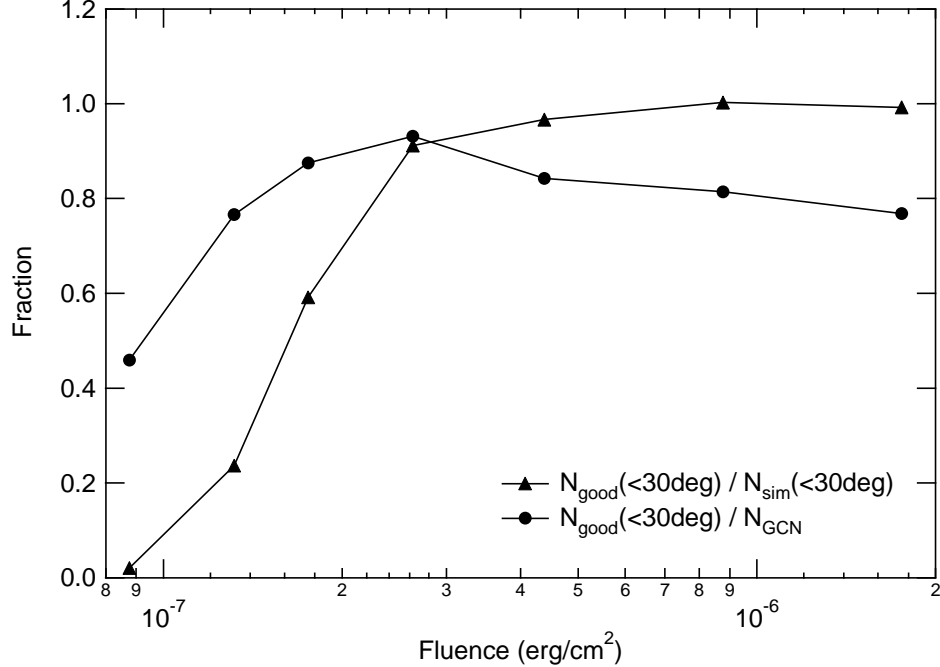


**Fig. 23.** Result from a flight localization simulation. The solid triangles show the fraction of correct localizations for events with incidence angles in the range  $\theta_{x,y} = -30^\circ$  to  $30^\circ$ , and for which GCN criterion 2, i.e. image SNR larger than 3.7, is satisfied. The solid circles show the fraction of correct localizations for events with the calculated incidence angle in the range  $\theta_{x,y} = -30^\circ$  to  $30^\circ$ , and for which GCN criterion 2 is satisfied.

## 6. Summary

We have calibrated the alignment between the WXM and the HETE-2 spacecraft aspect system. We estimate the systematic uncertainty of WXM locations of GRB to be  $2'$  for each X and Y direction at the 68% level. The corresponding two-dimensional systematic error is  $4'$  (90% confidence level). We calibrated the gain scale of the proportional counters using observations of the Crab Nebula and using the signal from the calibration radio-isotopes. At present, the systematic uncertainties in fitting a power-law spectrum model to the Crab spectrum are:  $\pm 0.1$ ,  $\pm 0.2 \times 10^{22} \text{ cm}^{-2}$  and 10% for power-law index, absorption column density, and absolute flux, respectively. Improvements in the spectral calibration are in progress. The in-orbit flight localization performance of the WXM was examined based on XRB observations and Monte Carlo simulations. The sensitivity of the flight localization is estimated to be  $> 10^{-7} \text{ erg cm}^{-2}$ , and the estimated false alert rate of real-time localizations is 20% for  $1.5 \times 10^{-7} - 2 \times 10^{-6} \text{ erg cm}^{-2}$ . Based on the recent GRB localizations, the rate of GRB localization is 28 per year, and the real-time localization rate is approximately one per month.

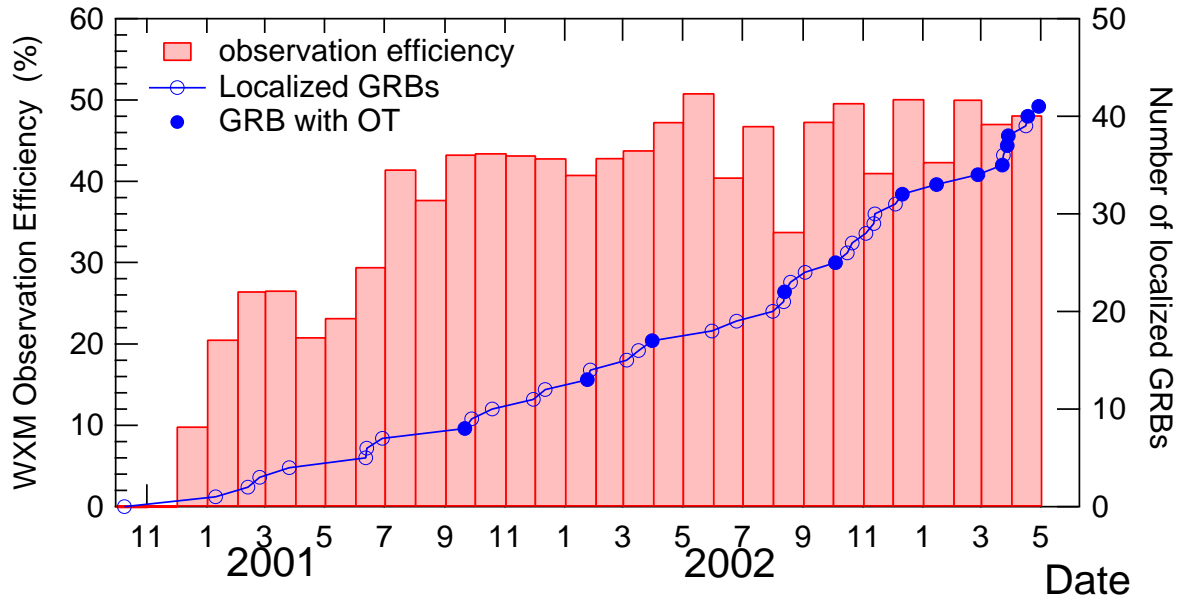


Fig. 24. Monthly operational efficiency and cumulative number of localized GRBs. The efficiency is defined by a fraction of the total HV on time in a month to the total time of the month. The GRBs for which optical transients are discovered are represented by solid circles.

## References

- Costa, E., et al., 1997, *Nature*, 387, 783
- Ricker, G. R., et al., 2003, in *AIP Conf. Proc. 662, Gamma-Ray Burst and Afterglow Astronomy 2001*, ed. G. R. Ricker and R. Vanderspek (New York: AIP), 3
- Atteia, J-L., et al., 2003, in *AIP Conf. Proc. 662, Gamma-Ray Burst and Afterglow Astronomy 2001*, ed. G. R. Ricker and R. Vanderspek (New York: AIP), 17
- Villasenor, J., et al., 2003, in *AIP Conf. Proc. 662, Gamma-Ray Burst and Afterglow Astronomy 2001*, ed. G. R. Ricker and R. Vanderspek (New York: AIP), 33
- Graziani, C., et al., 2003, in *AIP Conf. Proc. 662, Gamma-Ray Burst and Afterglow Astronomy 2001*, ed. G. R. Ricker and R. Vanderspek (New York: AIP), 114
- Shirasaki, Y., et al., 2003a, in *AIP Conf. Proc. 662, Gamma-Ray Burst and Afterglow Astronomy*, ed. G. R. Ricker and R. Vanderspek (New York: AIP), 117
- Shirasaki, Y., et al., 2003b, *Proc. SPIE, X-Ray and Gamma-Ray Telescopes and Instruments for Astronomy*, ed. J. E. Truemper and H. D. Tananbaum, 4851, 1310
- Shirasaki, Y., et al., 2000, *Proc. SPIE, X-Ray Optics, Instruments, and Mission III*, ed. J. E. Truemper and B. Aschenbach, 4012, 166
- Shirasaki, Y., et al., 2003c, *Proc. of Gamma Ray Bursts in the Afterglow Era — Third Workshop, Rome 17–20 September 2002*, in press.